The Astrophysical Journal, 1007:102 (18pp), 2026 August 20 https://doi.org/10.3847/1538-4357/ae8b97
© 2026. The Author(s). Published by the American Astronomical Society.
OPEN ACCESS

Rigorous Use of Light-curve Inversion and Stellar Occultation Techniques for Deriving a Scaled Three-dimensional Shape for the Jupiter Trojan (911) Agamemnon

Eros de O. Gradovski[1,2,3], Felipe Braga-Ribas[1,2,3,4], Altair R. Gomes-Junior[3,5], Bruno Sicardy[6], Jose Luis Ortiz[7], Giuliano Margoti[1,2,3], Chrystian L. Pereira[1,3], Pablo Santos-Sanz[7], Konrad Guhl[8], Josselin Desmars[6,9], Yucel Kilic[4,7], Nicolás Morales[7], Roberto Vieira-Martins[1,3], Rafael Sfair[6,10,11], Bruno Morgado[3,12], Julio I. B. de Camargo[1,3], Marcelo Assafin[3,12], Fabio A. Spina[2], Flavia Rommel[13], Gustavo Benedetti-Rossi[3], Jonatã Arcas-Silva[1,3], Luan M. Catani[7,12], Luana Liberato[14], Patricia Buzzatto[10], Thamiris de Santana[10], Vadim Nikitin[15], Jan Mánek[16], Mehmed N. Bağiran[17], Suleyman Fisek[18,19], Tim Haymes[8,20], Alberto J. Castro-Tirado[7,21], Alfonso Noschese[8,22], Alper K. Ates[23], Andrea Manna[8,24,25], Anna Marciniak[26], Antonio S. Amador[27], Carles Schnabel[8,28], Christine C. Gao[29], Christoph M. Schafer[30], Eda Sonbas[31], Faustino Organero[32], Fuat K. Yelkenci[18], Gregor Krannich[8], Ignacio de la Cueva[33], Jesús Castano[27], James Eisfeldt[15], Jean Bourgeois[34], Johnny Barton[35], Jose F. Águila[27], Jose L. Maestre[36], Karl-Ludwig Bath[8], Kevin Green[37], Leonor Ana[32], Malcolm Jennings[34], Maria Gritsevich[38,39], Martin Gutekunst[34], Mert Acar[23], Oguzhan Cakir[40,41], Olivier Schreurs[42], Peter Tickner[43], Roland Boninsegna[8], Selami Kalkan[44], Sinan Alis[18,19], Stefano Sposetti[8,24,25], Steve Messner[15], and Waldemar Ogloza[45]

[1] Observatório Nacional/MCTI, R. General José Cristino 77, CEP: 20.921-400, Rio de Janeiro, Brazil
[2] Federal University of Technology - Paraná (PPGFA/UTFPR-Curitiba), Av. Sete de Setembro, 3165, CEP 80230-901—Curitiba—PR, Brazil
[3] Laboratório Interinstitucional de e-Astronomia - LIneA, Av. Pastor Martin Luther King Jr. 126, CEP: 20765-000 Rio de Janeiro, RJ, Brazil
[4] LIRA, CNRS UMR8254, Observatoire de Paris, Université PSL, Sorbonne Université, Université Paris Cité, CY Cergy Paris Université, 92190 Meudon, France
[5] Universidade Federal de Uberlândia, Av. João Naves de Ávila, CEP 38408-100, MG, Brazil
[6] Laboratoire Temps Espace (LTE), Observatoire de Paris, Université PSL, CNRS UMR 8255, Sorbonne Université, LNE, 61 Av. de l'Observatoire, F75014 Paris, France
[7] Instituto de Astrofísica de Andalucía (IAA-CSIC), Glorieta de la Astronomía s/n, 18008 Granada, Spain
[8] International Occultation Timing Association–European Section (IOTA-ES), Am Brombeerhag 13, 30459 Hannover, Germany
[9] Institut Polytechnique des Sciences Avancées IPSA, 63 boulevard de Brandebourg, F-94200 Ivry-sur-Seine, France
[10] Universidade Estadual Paulista, Grupo de Dinâmica Orbital e Planetologia, Av. Dr. Ariberto Pereira da Cunha, 333, CEP: 12516-410, São Paulo, Brazil
[11] Department of Computational Physics, Institute for Astronomy & Astrophysics, University of Tübingen, Germany
[12] Universidade Federal do Rio de Janeiro. Observatório do Valongo, Ladeira Pedro Antônio 43, CEP 20080-090, RJ, Brazil
[13] University of Central Florida, Orlando, FL 32826, USA
[14] Université Côte d'Azur, Observatoire de la Côte d'Azur, CNRS, Laboratoire Lagrange, Bd de l'Observatoire, CS 34229, 06304, Nice Cedex 4, France
[15] International Occultation Timing Association, (IOTA-US), 2760 SW Jewell Avenue, Topeka, Kansas, USA
[16] Czech Astronomical Society, Occultation Section, Czechia
[17] Türksat Observatory–Türksat Company Headquarters Campus, Yaglipinar Mahallesi Türksat (Küme Evler) İdari Bina Apt. No:1, Gölbaşı, Ankara, Türkiye
[18] Department of Astronomy and Space Sciences, Faculty of Science, Istanbul University, 34116, Istanbul, Türkiye
[19] Istanbul University Observatory Research and Application Centre, 34116, Istanbul, Türkiye
[20] British Astronomical Association, PO Box 702, Tonbridge TN9 9TX, GB, UK
[21] Ingeniería de Sistemas y Automática, Universidad de Málaga, Unidad Asociada al CSIC por el IAA, Escuela de Ingenierías Industriales, Arquitecto Francisco Peñalosa, 6, Campanillas, 29071, Málaga, Spain
[22] AstroCampania ETS, via Servio Tullio 101, Napoli, Italy
[23] ISTEK Belde Observatory, Istanbul, Türkiye
[24] Società Astronomica Ticinese (SAT), c/o IRSOL, Via Patocchi 57, CH-6605 Locarno-Monti, Switzerland
[25] Schweizerische Astronomische Gesellschaft (SAG), Switzerland
[26] Astronomical Observatory Institute, Faculty of Physics and Astronomy, Adam Mickiewicz University, Słoneczna 36, 60-286 Poznań, Poland
[27] Orion Astronomical Association, USA
[28] Agrupació Astronòmica de Sabadell, Catalonia, Spain
[29] Columbia University, 550 W 120th Street, New York, NY 10027, USA
[30] Institute for Astronomy & Astrophysics, University of Tübingen, Germany
[31] Department of Physics, The George Washington University, Washington, DC 20052, USA
[32] Complejo Astronómico de La Hita, Camino de Doña Sol, s/n, 45850 LaVilla de Don fadrique, Spain
[33] Agrupación Astronómica de Eivissa (A.A.E.), C. Lucio Oculacio s/n, 07800 Eivissa, Spain
[34] Lucky Star observer collaborator, France
[35] Central Texas Astronomical Society (CTAS)14801 Farm to Market Road 182, Clifton, TX, USA
[36] Observatorio Astronómico de Albox, Albox, Almería, Spain
[37] University of New Haven Westport Astronomical Society, Westport, CT, USA
[38] University of Helsinki, FI-00014 Helsinki, Finland
[39] Institute of Physics and Technology, Ural Federal University, Mira str. 19, 620002, Ekaterinburg, Russia
[40] School of Mathematical and Physical Sciences, Macquarie University, Sydney, NSW 2109, Australia
[41] Astrophysics and Space Technologies Research Centre, Macquarie University, Sydney, NSW 2109, Australia
[42] Société Astronomique de Liège, Belgium
[43] University of Portsmouth, University House, Winston Churchill Avenue, Portsmouth, Hampshire PO1 2UP, UK
[44] Ondokuz Mayis University Observatory, Kurupelit Campus, 55139, Atakum/Samsun, Türkiye
[45] University of the National Education Commission, Krakow, ul. Podchorazych 2, 30-084 Kraków, Poland
Received 2025 December 27; revised 2026 July 9; accepted 2026 July 14; published 2026 August 11

Original content from this work may be used under the terms of the Creative Commons Attribution 4.0 licence. Any further distribution of this work must maintain attribution to the author(s) and the title of the work, journal citation and DOI.

Abstract

This work presents a methodology for determining the size, three-dimensional shape, and rotational parameters of small solar system objects, with rigorous uncertainty determination, using stellar occultations, rotational and phase-angle light curves. Here we analyze (911) Agamemnon, considered the third-largest Jupiter Trojan, using five rotational light curves, phase-angle data, and 12 occultations (22 positive chords). The methodology uses a genetic algorithm to compare the rotational data with synthetic light curves from the 3D model, obtaining the uncertainties from the χ^2 minimization. The model is scaled with the occultation data, to calculate dimensions, and the uncertainties. We obtained the first nonconvex model for Agamemnon using the All-Data Asteroid Modeling, considering new rotational, phase-angle, and occultation data. The methodological process was applied to derive the uncertainties, obtaining the rotational parameters $\lambda = 128.^{\circ}1 \pm 0.^{\circ}8$, $\beta = 2.^{\circ}3 \pm 2.^{\circ}1$, $P = 6.581797 \pm 0.000003$ hr, and $D_S = 156.0 \pm 7.8$ km, with a $\sigma_{\rm model}$ of 3 km (indicating the model quality relative to the occultation data). We also used the new data to test the 3D model provided by the Database of Asteroid Models from Inversion Techniques. From the nonconvex shape model rotated to Gaia observation epochs, we derive a geometric albedo of $p_G = 0.051 \pm 0.005$ for Agamemnon. The final results also indicate that (911) Agamemnon may be the second-largest known Jupiter Trojan, being smaller than (624) Hektor and larger than (617) Patroclus.

Unified Astronomy Thesaurus concepts: Jupiter trojans (874); Small Solar System bodies (1469); Solar system evolution (2293); Stellar occultation (2135)

1. Introduction

Populations of minor bodies can be located at different parts of the solar system. Jupiter Trojans (JTs) are a notable population of small bodies located at the L4 and L5 Lagrangian regions of Jupiter's orbit around the Sun (H. F. Levison et al. 1997). There are two main theories for the origin of these objects: the first is that they could have been captured as planetesimals during a growing proto-Jupiter phase (F. Marzari & H. Scholl 1998), in which case their characteristics would resemble those of inner solar system bodies. The second is that they could have been formed in the outer solar system and captured during Jupiter's early planetary migration (R. Gomes et al. 2005; A. Morbidelli et al. 2005; K. Tsiganis et al. 2005). More recent models aim to explain the asymmetry in the number of minor bodies between the L4 and L5 regions. D. Nesvorný et al. (2013) and J. Li et al. (2023) suggest that the Trojans were captured during the "Jumping Jupiter" phase, when Jupiter's orbit suddenly changed due to its interactions with other gas giants. Studying the rotational parameters and physical properties of these bodies can provide insights into their origins and their similarities with other solar system objects. With the aim to better characterize the Trojans' topography, determine their composition, derive masses, density, and search for satellites or rings around a few objects (H. F. Levison et al. 2021), the National Aeronautics and Space Administration (NASA) organization launched a spacecraft on 2021 October 16, called Lucy Mission (C. B. Olkin et al. 2021). Ring systems were already found around Centaurs (F. Braga-Ribas et al. 2014; C. L. Pereira et al. 2025) and Trans-Neptunian objects (TNOs; J. L. Ortiz et al. 2017; B. E. Morgado et al. 2023; C. L. Pereira et al. 2023), but they were never found among Trojans or main belt asteroids (MBAs). In contrast, satellites were already found in the Trojan region (B. Timerson et al. 2013; F. Marchis et al. 2014; K. S. Noll et al. 2020). Although the Lucy Mission will provide a wealth of information about the JTs, it will only visit a limited number of objects. To fully comprehend this class, different observational approaches are necessary.

The stellar occultation technique is a powerful method for obtaining information about JTs through ground-based observations. This technique involves observing the body's passage in front of a star, as seen from a specific location. What the observer registers is the variation of the target star flux during the event time, caused by the object's passage. As the position of the star and the object's velocity are well known, the duration of the event can be translated into the projected size of the body along the observer's path, known as an occultation chord (B. Sicardy et al. 2024). In particular, the Jupiter Trojan (911) Agamemnon, located in the L4 region and currently known as the third-largest known Trojan, after (624) Hektor and (617) Patroclus (T. Grav et al. 2012), has been the target of several stellar occultations in recent years (Section 2.2). On 2012 January 9, a stellar occultation by Agamemnon revealed a satellite as presented by B. Timerson et al. (2013). Several rotational light curves (LCs), which consist of observing the object's flux variation with time caused by its rotation, were also obtained for Agamemnon in the past years (Section 2.1).

In this work, we obtained new data and tested it against Agamemnon's three-dimensional model, as provided in the literature, to evaluate its quality (Section 3). We have also used stellar occultations, solar phase angle, and rotation light-curve observations to simultaneously derive a nonconvex shape model and better constrain its size, shape, and rotational parameters (Section 4). Along with the 3D shape determination, we have also developed a methodology to rigorously determine the uncertainties of the rotational and shape parameters.

2. Agamemnon's Datasets

2.1. Rotational and Solar Phase Angle Light Curves

Rotational light curves, derived from multiple observations over the object's rotation period, and solar phase angle light curves, obtained from sparse brightness measurements at different phase angles, can provide information about the object's pole orientation, rotation period, rotational phase, and photometric phase-function parameters. To better constrain these properties for Agamemnon, we obtained a rotational light curve in 2020 July using the Boller&Chivens 0.6 m telescope with an Ixon 4335 CCD at Pico dos Dias Observatory (OPD) in Brazil, operated by the National

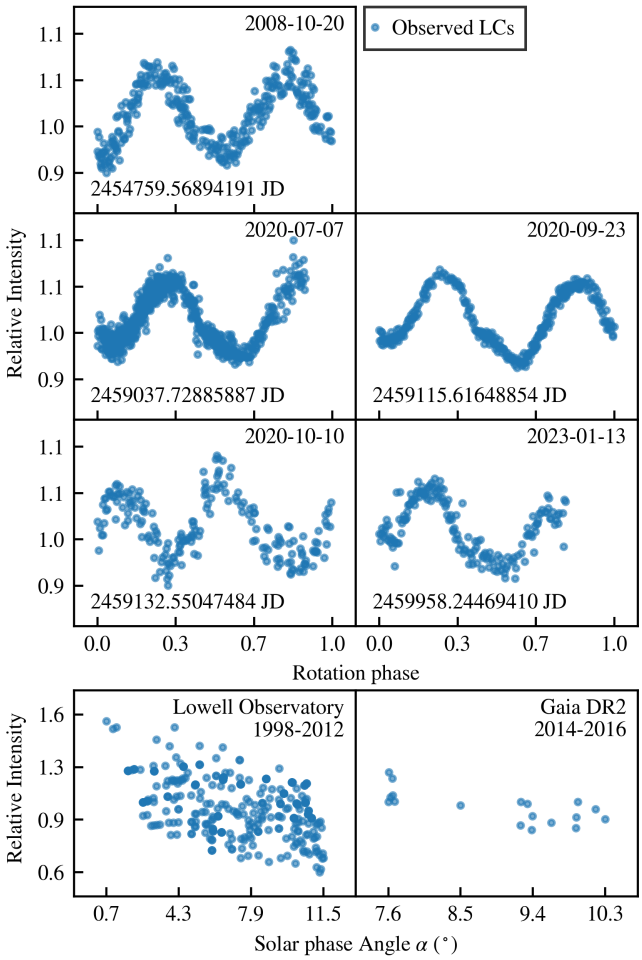


Figure 1. Rotational and solar phase angle light curves for Agamemnon are presented. The top section displays all the rotational light curves, including the 2020 July curve obtained at the Pico dos Dias observatory. The Julian dates indicate the initial phase of each curve, with a rotation period of 6.581800 hr used to determine the phase. The bottom section presents the phase angle light curves obtained from Gaia and Lowell.

Laboratory of Astrophysics (LNA). The images were analyzed using the Package for the Reduction of Astronomical Images Automatically (PRAIA; M. Assafin 2023). PRAIA performs differential aperture photometry, in which several reference stars in the field are selected to compare their fluxes with that of the target object. By dividing the body's flux by the reference stars, we obtain the variations caused by the different faces of the body reflecting the Sun's light.

Other rotational light curves for this object were available at the Asteroid Light Curve Data Exchange Format (ALCDEF) database (R. D. Stephens 2009; T. Polakis 2021; R. D. Stephens & B. D. Warner 2021), resulting in a total of five rotational light curves from 2008 up to 2023. Solar phase angle curves, which consist of measuring Agamemnon's reduced magnitude at different Sun-to-Earth angles, were also available in Gaia Data Release 2 (DR2; Gaia Collaboration et al. 2018) and by the Lowell Observatory database that uses photometry of ground-based surveys reported to the Minor Planet Center (D. Oszkiewicz et al. 2011; E. Bowell et al. 2014; J. Ďurech et al. 2019) (Figure 1). All curves were normalized to a relative intensity and light time corrected.

2.2. Stellar Occultations

A total of 12 new stellar occultation events by (911) Agamemnon were successfully observed from 2020 to 2025. The event predictions were provided by the Lucky Star[46] project, using the Numerical Integration of the Motion of an Asteroid ephemeris (NIMA; J. Desmars et al. 2015), and the occultation images were reported by the observers to the Occultation portal[47] (Y. Kilic et al. 2022).

The stellar occultation images were analyzed using the differential aperture photometric process implemented with the PRAIA package. By dividing the target's flux by the reference stars' flux, the analysis mitigates variations caused by changes in sky transparency, isolating the flux variation attributed to the occultation.

To obtain the immersion and emersion times from each light curve, the Stellar Occultation Reduction Analysis (SORA; A. R. Gomes-Júnior et al. 2022) Python package was used. SORA considers the apparent star diameter, event velocity, image exposure time, and Fresnel diffraction to model the occultation light curve and thus precisely determines the event ingress and egress. This generates a light-curve model that can be compared to the observed curve. Considering the event velocity, occultation instants, and observers' positions, the occultation chords can be obtained, which are representations of a sized section of the body obtained for each observer.

A total of 22 positive detections (chords) from different sites were obtained, involving professional and amateur astronomers. These resulted in seven positive single-chord events, three double chords, one event with three chords, and one with six chords. The stars and observers' information for each event, and the stellar occultation light curves obtained from each site, are presented in the Appendix.

2.3. Three-dimensional Model from Light-curve Inversion

The object's three-dimensional shape and rotational state can be derived using the light-curve inversion technique developed by M. Kaasalainen & J. Torppa (2001), M. Kaasalainen et al. (2001). The method fits disk-integrated rotational light curves by adjusting a parameterized shape model together with the spin parameters. Starting from an initial shape, typically an ellipsoid, the model is numerically illuminated according to a chosen scattering law to compute synthetic light curves. The solution is obtained by minimizing a nonlinear cost function composed of a data-fitting term, which measures the agreement between observed and synthetic light curves, and a regularization term, which ensures smoothness and stability of the shape model. The shape and rotational parameters are iteratively optimized until convergence is reached. The reliability of the solution improves when light curves covering a wide range of aspect and phase angles are used.

In order to generate a 3D model, different software can be used, such as the shaping asteroid models using genetic evolution (SAGE; P. Bartczak & G. Dudziński 2018), Convexinv[48] (J. Durech et al. 2010), All-Data Asteroid Modeling (ADAM; M. Viikinkoski et al. 2015), and the Knitted Occultation, Adaptive-optics, and Lightcurve Analysis (KOALA; M. Kaasalainen & L. Lamberg 2006; B. Carry et al. 2010).

[46] https://lesia.obspm.fr/lucky-star/
[47] https://occultationportal.org
[48] https://astro.troja.mff.cuni.cz/projects/damit/pages/software_download

Table 1
Agamemnon's 3D Model Parameters Provided by DAMIT Database, Where λ is the Ecliptic Pole Longitude, β the Pole Latitude, ϕ_0 the Initial Rotation Phase Angle at the Reference Date t_0, P the Rotation Period and A_0, D and k the Amplitude, Width, and Slope of the Phase Function

λ (deg)	A_0	P (hr)
β (deg)	D	$t0$ (JD)
$\phi 0$ (deg)	k	
126	0.67	6.58179
0	0.01	2451091
0	−1.4	

Note. λ is the ecliptic pole longitude, β is the pole latitude, ϕ_0 is the initial rotation phase angle at the reference date t_0, P is the rotation period, and A_0, D, and k are the amplitude, width, and slope of the phase function.

Both SAGE and Convexinv use only rotational light curves to generate 3D models.

A few databases provide three-dimensional models for solar system small bodies.[49,50,51,52] The Database of Asteroid Models from Inversion Techniques (DAMIT; J. Durech et al. 2010) is one of the most popular. DAMIT's models can be generated using various types of datasets, including rotational light curves, solar phase angle light curves, stellar occultation data, adaptive optics images, and direct images obtained by spacecraft. However, most available models use only rotational and solar phase angle light curves, resulting in a convex unscaled 3D model. These models provide an overall view of the object's shape, but do not scale it to its actual size. This also applies to (911) Agamemnon, for which the DAMIT model was obtained based on Gaia DR2 photometry and Lowell Observatory photometric database curves (J. Durech et al. 2019), resulting in two phase angle curves, from 1998 to 2012 (Lowell Observatory) and from 2014 to 2016 (Gaia DR2). The parameters provided for this model are shown in Table 1.

3. Determination of Phase, Rotational, and Dimensional Parameters with Uncertainties

The uncertainties of the three-dimensional models obtained from the inversion technique are not directly available. In this section, we present a methodology we developed to determine the 3D model's pole orientation, rotation period, phase parameters, and scale, with their corresponding uncertainties. From the resulting values, the surface-equivalent and volumetric diameters are also calculated.

3.1. Constraints from Rotational Light Curves and Solar Phase Angle Data

As several databases offer 3D models of asteroids, and new data is constantly being collected, it is natural to first compare these models with the new data to assess their uncertainties, rather than directly creating a new model.

In this scenario, given an initial 3D model, a synthetic light curve can be generated from its shape and compared with observed light curves to estimate the model's uncertainties.

[49] https://astro.troja.mff.cuni.cz/projects/damit/
[50] http://isam.astro.amu.edu.pl/
[51] https://3d-asteroids.space/
[52] https://sbn.psi.edu/pds/shape-models/

The rotation phase angle (ϕ) at the observation date t, pole orientation (λ, β), and rotation period (P) are the parameters that are best constrained by the rotational and solar phase angle light curves.

To calculate the object's figure in the sky plane at a specific date, we use the model's poles and determine its rotation phase using

$$\phi = \phi_0 + \omega(t - t_0), \tag{1}$$

where ϕ_0 is the phase at a reference date t_0, and ω is the rotation velocity that can be written as $360°/P$

The model's flux follows the Lambert Lommel–Seeliger scattering function (M. Kaasalainen et al. 2001; P. Bartczak & G. Dudziński 2018)

$$S_{(\mu,\mu_0,\alpha)} = f_{(\alpha)}\left[(1 - c)\frac{\mu\,\mu_0}{\mu + \mu_0} + c\,\mu\,\mu_0\right], \tag{2}$$

where μ is the cosine of the angle between the surface normal and the direction of the Earth, μ_0 is the cosine of the angle between the surface normal and the Sun, and c is a weight factor that gives the proportion between the Lommel–Seeliger part of the equation $\left((1 - c)\frac{\mu\,\mu_0}{\mu + \mu_0}\right)$ and the Lambertian part ($c\,\mu\,\mu_0$). In this case we adopted c as 0.1 resulting in a 10% Lambertian component and 90% Lommel–Seeliger.

The $f_{(\alpha)}$ factor represents the solar phase angle function

$$f_{(\alpha)} = A_0 e^{\left(-\frac{\alpha}{D}\right)} + k\alpha + 1, \tag{3}$$

where A_0 is the amplitude and D the width of the opposition effect, while k is the slope of the phase function, representing the brightness variation at different phase angles (α). It is important to note that, if no solar phase angle data is available, the f_α factor can be assumed to be 1, as no flux variation due to solar phase variation can be considered. Also, this law provides the reflected flux of each facet in the shape model. The total flux for a given date is obtained by summing only the facets that are illuminated by the Sun, visible from Earth, and not blocked by other parts of the body.

With these considerations, a synthetic representation of the rotational and solar phase angle light curves can be generated and compared to the observed ones. Figure 2 shows a comparison between the observed data and synthetic light curves generated using DAMIT's model and assuming its nominal values for the rotation parameters (Table 1).

To assess the model's uncertainty, different combinations of each variable (λ, β, ϕ_0, P, A_0, D, and k) are used to generate synthetic light curves. The synthetic curves were compared to the observed data points using the chi-squared (χ^2) test:

$$\chi^2 = \sum_{i=1}^{N} \frac{(O_i - S_i)^2}{\sigma^2}, \tag{4}$$

where N is the number of points of each light curve, O_i the observed values, S_i the synthetic values and σ the uncertainty associated with each observed value. Since some ALCDEF light curves do not include individual photometric uncertainties, the light-curve dispersion was adopted as the overall σ for those observations. The χ^2 value for each combination of parameters is saved, so the best set of values can be determined.

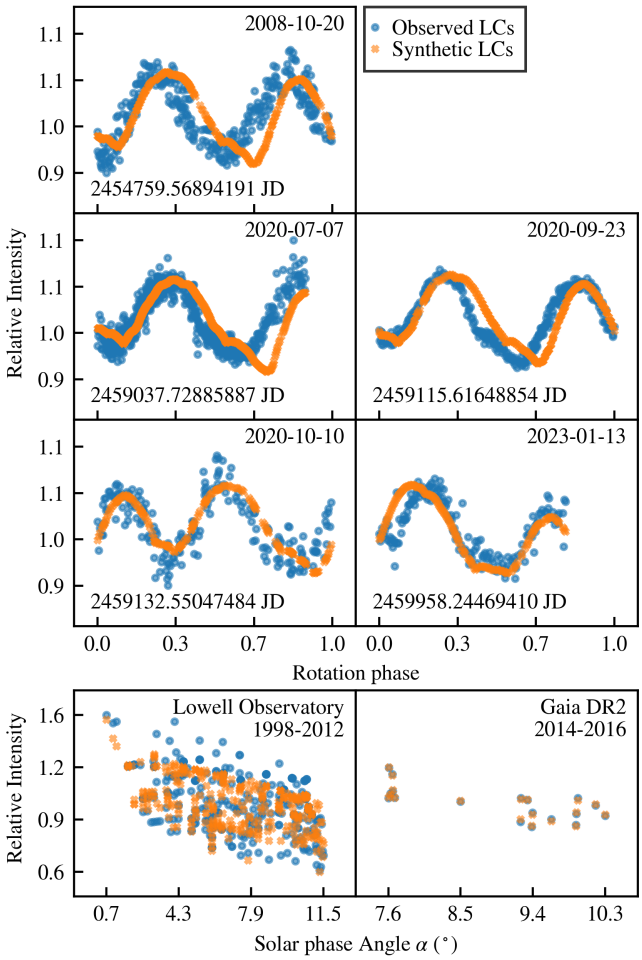


Figure 2. Representation of synthetic light curves (orange) compared to observed ones (blue) using DAMIT's nominal parameter values. The initial time of each rotational light curve is represented as a Julian date, and the rotation phase from 0 to 1 considers the proposed period of 6.58179 hr from DAMIT. The solar phase angle light curves show better agreement, as they were the ones used to generate the model.

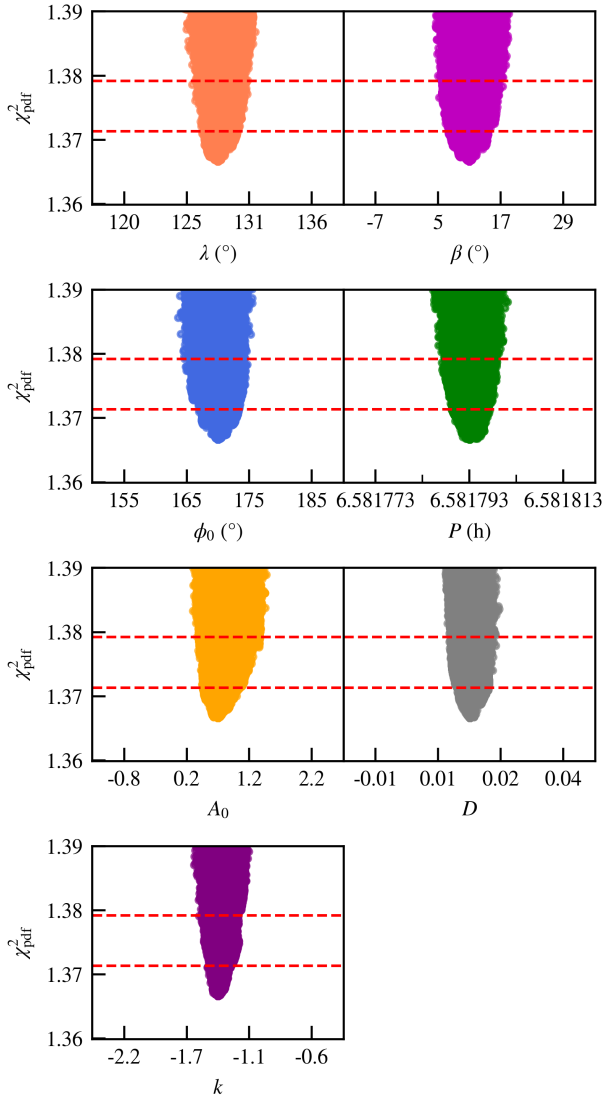


Figure 3. Resulting χ^2 test considering the observed and synthetic light curves. Each point represents a different combination of λ, β, ϕ_0, P, A_0, D, and k, where the χ^2 closer to 1 represents the best fit. The red dashed lines represent the 1σ and 3σ uncertainty regions.

Instead of using the reference date presented by DAMIT (2451091 JD) as the reference epoch for the initial phase angle (ϕ_0), we adopted a new reference date close to the maximum in brightness intensity of the Pico dos Dias Observatory light curve, on 2020 July 7, resulting in 2459037.8142284 JD.

This date was chosen to minimize the uncertainty of the phase angle (ϕ), caused by the propagation of the rotation period uncertainty, from the original date to the epoch of the new rotational light curves and occultation events.

To determine the global minimum and its uncertainty while avoiding local minima, the following intervals were considered for each variable: $\lambda = 180 \pm 180$, $\beta = 0 \pm 90$, $\phi_0 = 0 \pm 180$, $P = 6.58179 \pm 0.001$ h, $A_0 = 1 \pm 4$, $D = 0 \pm 0.5$, and $k = 0 \pm 5$. The minimum χ^2 region obtained as a function of each parameter are shown in Figure 3.

The uncertainties on the fitted parameters were estimated using the $\Delta\chi^2$ criterion, considering the joint confidence region of all free parameters simultaneously. The corresponding $\Delta\chi^2$ thresholds were obtained from the percent point function (χ^2_{ppf}) of the χ^2 distribution, which returns the $\Delta\chi^2$ value associated with a given cumulative confidence level and the number of free parameters considered. For the rotation light curves and sparse photometric data, seven free parameters were fitted (λ, β, ϕ_0, P, A_0, D, and k). The 1σ and 3σ confidence regions correspond to cumulative probabilities of 68.27% and 99.73%, respectively.

The resulting values within the 1σ region obtained for the model are presented in Table 2. Comparing these results with the parameters proposed by DAMIT (Table 1), we note that only β presents a slightly higher value, within its uncertainty. The difference in ϕ_0 is due to the chosen new reference date, which changes the initial phase angle.

The process of generating synthetic light curves and comparing them with observed data can require considerable computational resources. To minimize the processing time, genetic algorithms and parallel processing were implemented (F.-A. Fortin et al. 2012). The genetic algorithm (GA) tries to simulate the processes of natural selection. The GA operates on a population by selecting the fittest individuals, which in this context are those with the lowest χ^2. These individuals are then paired to perform the crossover of their "genomes," which, in this context, are the model's variables, such as the

Table 2
Resulting 1σ Uncertainty Range Obtained for the Comparison between the Synthetic Light Curves Generated Using Agamemnon's 3D Model Proposed by DAMIT and the Real Solar Phase Angle and Rotational Light Curves

λ (deg)	A_0	P (hr)	$\chi^2_{\rm pdf}$
β (deg)	D	t_0 (JD)	(minimum)
ϕ_0 (deg)	k		
128.0 ± 1.5	0.78 ± 0.29	6.581793 ± 0.000004	1.36
10.8 ± 3.8	0.015 ± 0.004	2459037.8142284	
170.3 ± 3.1	−1.39 ± 0.10		

rotation period. This process generates the new population where, once again, the individuals with the lowest χ^2 are selected. This methodology ensures that only the best combinations of variables survive the test, leading the result to converge toward a minimum. Random mutations are implemented at each generation, preventing the algorithm from falling into local minima. If the algorithm finds a more promising region with the mutation, this will become the new region to be populated.

3.2. Constraints from Stellar Occultation Data

Stellar occultation chords are able to provide measurements of the object's limb with a kilometric accuracy. Therefore, it can be used to determine the scale of an object's 3D model. It may also constrain the rotation parameters (A. R. Gomes-Júnior et al. 2019).

The 3D model must be rotated to the epoch of each occultation event using Equation (1). The chord extremities are then compared to the projected limb (A. R. Gomes-Júnior et al. 2022).

To determine the object's scale, each parameter (λ, β, ϕ_0, and P) is varied within the uncertainty range. Different sets of the rotation parameters, scale values, and stellar occultation centers are used to orient the object's model. The limb is then compared to the chords' extremities using the chi-squared ($\chi^2_{\rm occ}$) test:

$$\chi^2_{\rm occ} = \sum_{i=1}^{N} \frac{(r_{\rm i,chord} - r_{\rm i,model})^2}{\sigma^2_{\rm i,chord} + \sigma^2_{\rm model}}, \quad (5)$$

where $(r_{\rm i,chord} - r_{\rm i,model})$ is the radial difference between the chord extremity and the model limb, $\sigma_{\rm i,chord}$ is the chord extremity uncertainty, and $\sigma_{\rm model}$ is a limit to the model resolution (in kilometers; F. L. Rommel et al. 2023).

A perfect model would have $\sigma_{\rm model}$ equal to zero, but in general, models are approximate representations of the object's global shape. Stellar occultations, on the other hand, provide very precise measurements of the object's true limb. So, when fitting the chords to the models, a discrepancy between the two is natural. Thus, the $\sigma_{\rm model}$ allows for accommodating the model to occultation chords, which can also be understood as an indication of the quality of the used model, as high values of this variable can indicate that the model has no agreement with the occultation data. The minimum $\sigma_{\rm model}$ necessary to obtain chi-squared per degree of freedom ($\chi^2_{\rm occ\ \ pdf}$) close to unity, indicating a good fit, is used to determine the uncertainties of the scale and rotation parameters.

The fit of the occultation chords is determined jointly from all available data. Here we used the rotation parameters and the respective limits obtained with the χ^2 test (Section 3.1, Table 2). Even if, in most cases, fitting the model to single-chord events results in negligible $\chi^2_{\rm occ}$ values, these events were also considered, as large single-chord events can impose constraints on the model's scale. The 2023 February occultation is a good example, being a long chord with small uncertainties.

In this case, the processing time was also quite long, so, as for the light-curve tests, the genetic algorithm and parallel processing were also implemented.

The results obtained for Agamemnon's 3D model are shown in Table 3, where, similarly to the rotation light curves, the uncertainties were estimated using the $\Delta\chi^2$ criterion.

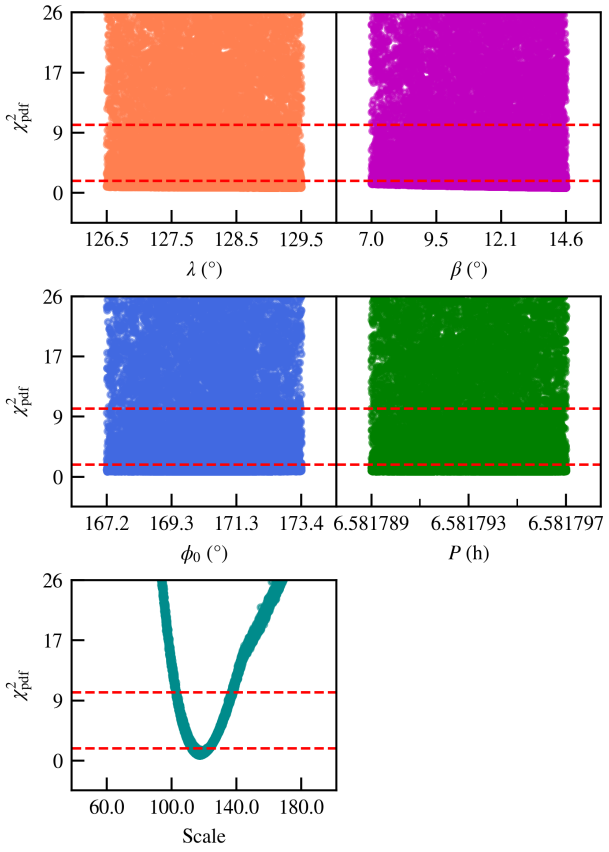


Figure 4. Resulting $\chi^2_{\rm occ\ \ pdf}$ graphs considering the stellar occultation chords and the 3D model. The limit of search for each variable was defined by the χ^2 test with the new rotational light curves, where, in this case, the occultations restricted the model scale. On the other hand, the remaining variables are not further restricted, with all the results being below the 1σ line.

Table 3
Results Obtained for the 1σ Region When Comparing the Occultation Chords with the Model's Limb

Scale factor	D_V (km)	D_S (km)	Volume (10^6 km^3)	$\sigma_{\rm model}$ (km)	$\chi^2_{\rm occ\ \ pdf}$
117.8 ± 5.8	146.2 ± 7.2	152.0 ± 7.5	1.65 ± 0.24	3.0	0.9

Note. A scale factor, volumetric-equivalent diameter (D_V), surface-equivalent diameter (D_S), and volume could be determined using the stellar occultation data.

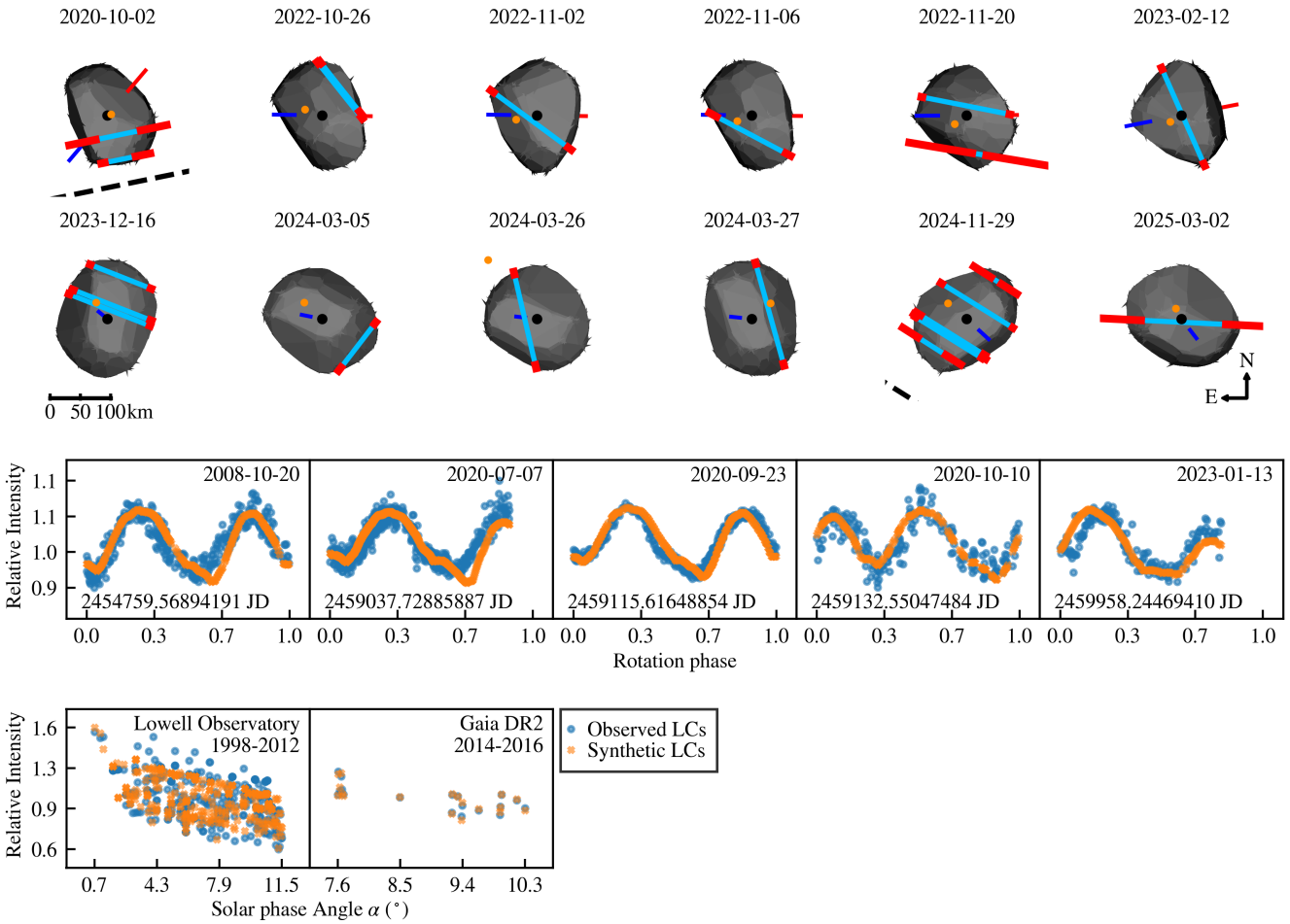


Figure 5. Best fit obtained for Agamemnon's 3D model provided by DAMIT, considering all the stellar occultation events, rotational and solar phase angle light curves. The blue lines with red bars at their extremities represent the stellar occultation chords with their uncertainties. The dark blue and red lines originating from the model center represent its pole orientation. The orange dot represents the predicted center for the occultation, and the black dot the model's fitted center. All adjustments were made considering the same rotational parameters and scale for the body. The Julian dates represent the initial phase of each light curve, where the best period of 6.581791 hr was considered as a complete rotational phase.

However, in this case, only one free parameter was fitted, since only the scale was constrained. The $\chi^2_{\text{occ pdf}}$ plots for each parameter can be seen in Figure 4, where a σ_{model} of 3 km was needed in order to obtain a $\chi^2_{\text{occ pdf}}$ close to 1. As can be noted by the flat $\chi^2_{\text{occ pdf}}$ at the bottom of the rotation parameters variables, no further constraints were obtained when the occultation chords were considered. The results, along with the calculated uncertainties are those presented in Table 2. The final visualization of the best fit, considering all stellar occultation events and rotational light curves simultaneously, can be seen in Figure 5.

4. A Nonconvex Model for Agamemnon

Since Agamemnon's 3D shape model provided by DAMIT does not satisfactorily reproduce the new stellar occultations and rotational light curves, we derived a new 3D model using the ADAM software (M. Viikinkoski et al. 2015).

The ADAM software simultaneously considers occultation chords and rotational light curves to generate the model. The light-curve inversion technique adopted in ADAM is described in M. Viikinkoski et al. (2015), where the final result should agree with both stellar occultations and rotational light curves, thereby yielding a model already scaled by the occultation chords.

To obtain a model that satisfactorily fits all data, several shapes were generated using ADAM, adopting the octanoid parameterization and the Lambert Lommel–Seeliger scattering function. The phase parameters were fitted, and multiple axis sizes, weight factors, and pole combinations were tested. These tests indicated that the pole orientation, rotational period, and scale remained very stable when the initial guesses were changed. The overall shape remained very similar, although variations in the convexity, light curve, and occultation weights produced alternative solutions with slightly different features, ranging from a steeper to a rounded version of the model. The best model for Agamemnon was selected based on the lowest χ^2 values obtained with ADAM for each observational technique, as well as on the final combined χ^2 value. This solution kept the light curve weight at 7 and the occultation weight at 0.06, where the initial ellipsoid had the semiaxes $a = 150$ km, $b = 120$ km, and $c = 80$ km.

ADAM provides only the final model and the best rotation parameters. Therefore, no uncertainty is available for these parameters. In order to determine the model's uncertainties, the same tests between real and synthetic light curves and

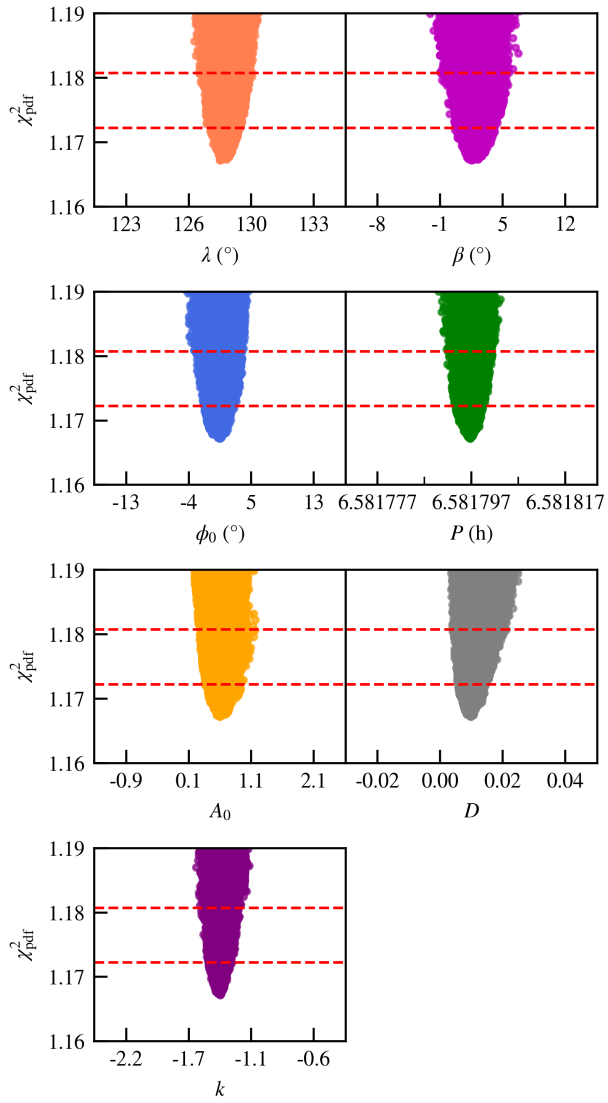


Figure 6. Results obtained comparing the synthetic light curves generated by Agamemnon's model made with ADAM, and the real light curves. Here, the tendency of each parameter is clear, making it possible to determine the model uncertainties, where the red dashed lines represent the 1σ and 3σ regions.

comparison between model limb and chords extremities described in Section 3 were applied, where each parameter was varied considering the following ranges to avoid local minima: $\lambda = 180 \pm 180°$, $\beta = 0 \pm 90°$, $\phi_0 = 0 \pm 180°$, $P = 6.581797 \pm 0.001$ hr, $A_0 = 0.59 \pm 5$, $D = 0.014 \pm 1$, and $k = -1.39 \pm 5$.

Generating the synthetic light curves using ADAM's 3D model and comparing them with the observed data allows us to determine the rotation and reflection parameters uncertainties, using the χ^2 test. Figure 6 presents the χ^2_{pdf} graphs around the global minimum and Table 4 the derived values and uncertainties.

Here we adopted the same reference date used in Section 3.1 (2459037.8142284 JD), which is close to the maximum relative intensity of the light curve observed at Pico dos Dias Observatory on 2020 July 7.

Considering the χ^2 uncertainties, determined with the rotational light curves, and applying the χ^2_{occ} test between

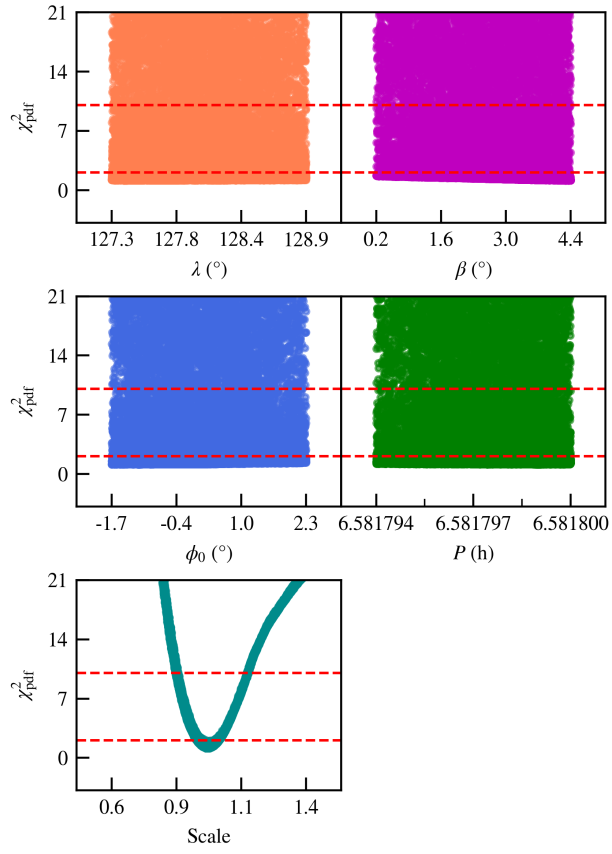


Figure 7. Resulting $\chi^2_{occ\ pdf}$ obtained for Agamemnon's model generated with ADAM.

Table 4
Results Obtained for the 1σ Region Considering Agamemnon's Model Generated with ADAM

λ (deg)	A_0	P (hr)	χ^2_{pdf}
β (deg)	D	t_0(JD)	(minimum)
ϕ_0 (deg)	k		
128.1 ± 0.8	0.65 ± 0.28	6.581797 ± 0.000003	1.17
2.3 ± 2.1	0.014 ± 0.004	2459037.8142284	
0.3 ± 2.0	−1.39 ± 0.10		

the chords extremities and Agamemnon's nonconvex 3D model limb, we obtain the $\chi^2_{occ\ pdf}$ graphs presented in Figure 7. A σ_{model} of 3.0 km was needed to have a global $\chi^2_{occ\ pdf}$ close to unity. As ADAM already scaled the body in the generation process, a scale of 1 represents the best solution found. No further constraints on the rotation parameters are obtained when fitting the occultation chords. Table 5 presents the surface-equivalent and volumetric diameters. The chords fitted to the model, as well as the comparison between the synthetic and observed light curves, are shown in Figure 8, where the same rotation parameters and scale were applied.

The derived model also rules out the opposite-pole solution, as it fails to fit the 2024 November stellar occultation chords when the model's projected limb is considered, resulting in an unambiguous pole solution for the model.

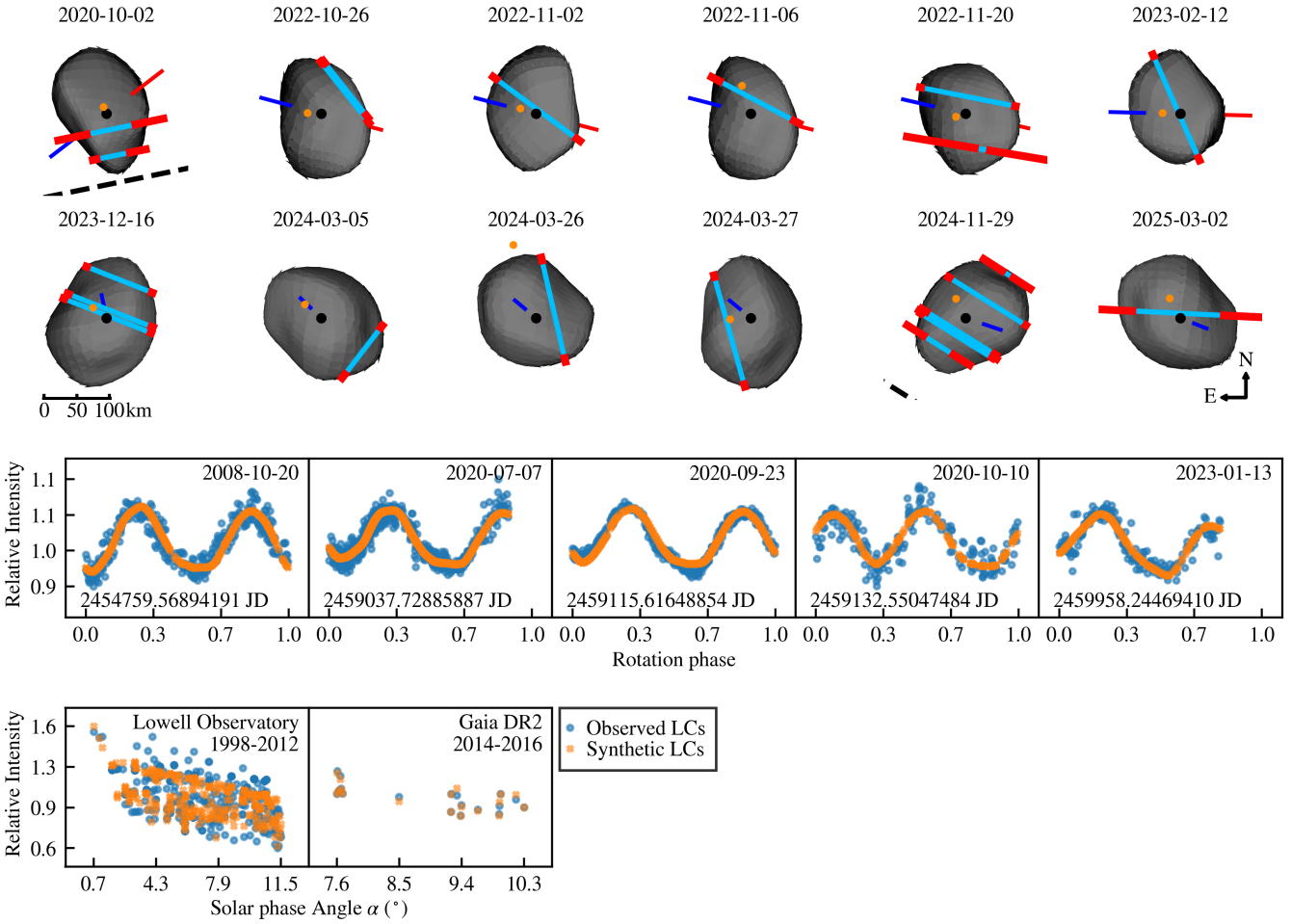


Figure 8. Similar to Figure 5 but for our final 3D model for (911) Agamemnon, generated with ADAM. The superior part of the figure shows the stellar occultation chords fitted to the model limb, and the bottom part shows the synthetic light curves compared with the real ones. The same rotation parameters and scale were adopted for all cases. The period considered for one complete rotation phase was 6.581797 hr.

Table 5
Final Results Obtained for Agamemnon's Model Generated Using ADAM

Scale Factor	D_V (km)	D_S (km)	Volume (10^6 km^3)	$\sigma_{\rm model}$ (km)	$\chi^2_{\rm occ\ pdf}$
1.00 ± 0.05	151.3 ± 7.6	156.0 ± 7.8	1.83 ± 0.3	3.0	1.0

Note. These values correspond to the 1σ region, restricting the body's size.

5. Geometric Albedo

We can use the nonconvex model derived from the stellar occultation, rotational light curves, and phase angle data to calculate the object's geometric albedo using the following equation (B. Sicardy et al. 2011):

$$p_{\rm V} = \left(\frac{1\,{\rm AU}}{R_{\rm S}}\right)^2 10^{0.4(H_{\odot,{\rm V}} - H_{\rm V})}, \quad (6)$$

where 1 au $\sim 1.49598 \times 10^8$ km $H_{\odot,{\rm V}}$ is the Sun's absolute magnitude at V band (~ -26.76), $H_{\rm V}$ Agamemnon's absolute magnitude in the V band and $R_{\rm S}$ the surface-equivalent radius of the body.

Considering the obtained nonconvex model surface-equivalent radius $R_{\rm S} = 78.0 \pm 3.9$ km (Table 5), Agamemnon's absolute magnitude of 7.89 obtained by T. Grav et al. (2012), and the Sun's magnitude of -26.76 (C. N. A. Willmer 2018), we obtain a $p_{\rm V} = 0.051 \pm 0.003$. Using WISE infrared observations, T. Grav et al. (2012) determined a geometric albedo of 0.072 ± 0.010 considering an equivalent diameter of 131.04 ± 1.19 km. Note that the authors did not consider an uncertainty for the absolute magnitude in their results.

A more rigorous approach to deriving the geometric albedo should account for the object's illuminated surface, considering the solar phase angle and aspect angle at the exact epochs when the magnitude was measured. For Agamemnon, this can be achieved by rotating the 3D model to the dates of Gaia's observations and computing the albedo from the corresponding reduced magnitude and its uncertainty, i.e., the surface-equivalent area of the illuminated facets and its associated uncertainty due to the model scale variation. Here we adopted the Solar G-band magnitude, $G_\odot = -26.9$, from L. Casagrande & D. A. VandenBerg (2018).

This procedure provides an individual geometric albedo estimate for each of the 18 Gaia observation epochs, which can be combined, resulting in a mean value and a range of $p_{\rm G} = 0.051 \pm 0.016$. Considering that this range is dominated

by a scatter on Gaia data, we consider the standard deviation as our final uncertainty, resulting in a reduced magnitude of 8.611 ± 0.112 and geometric albedo of $p_G = 0.051 \pm 0.005$.

Therefore, the difference between our results and those of T. Grav et al. (2012) may be related to differences in the phase angle, the aspect angle at the time of the observations, and the applied solar magnitude. In addition, our analysis considers only the illuminated facets of a three-dimensional shape model, while T. Grav et al. (2012) uses an elliptical shape.

6. Discussion

As discussed in Sections 3.1 and 3.2, model uncertainties can be constrained using stellar occultations, rotational light curves, and solar phase angle data. If data from only one of the above techniques is available, it can still be used to constrain the object's parameters and associated uncertainties. However, when multiple datasets are available, they can be combined in a joint analysis to provide stronger constraints. For Agamemnon, the availability of data from all three techniques enabled a full analysis.

Considering the final result obtained for (911) Agamemnon with DAMIT's model (Table 3 and Figure 5), it can be seen that the model provides a reasonable representation of the object's shape, and the synthetic light curves present an overall contour that agrees with the new data. Nevertheless, the 2020 July and 2023 January light curves do not fit well. The occultation events of 2023 February and 2023 December also fail to have a good fit. One of them tends to a bigger scale while the other suggests a smaller one. The global σ_{model} of 3 km indicates that the overall fit is acceptable as the model is intended to represent an overall shape of the body.

The results obtained for the new nonconvex model generated with ADAM (Table 5 and Figure 8) show an improvement in the body's representation. The main difference occurs in the rotational light curves, where it is possible to notice in Figures 5 and 8 that the nonconvex model fits best, resulting in a minimum χ^2_{pdf} of 1.17 compared with 1.36 for the DAMIT model.

Using the 3D model and Gaia observations, we determined an accurate albedo for Agamemnon. The model was rotated to the epochs of Gaia's observations of Agamemnon, and the measured reduced magnitudes were used to determine its geometric albedo, accounting for aspect and solar phase angles to compute the actual illuminated surface area. As discussed, using different Gaia observations, we obtained a mean albedo of 0.051 ± 0.005, but the values can vary by almost 31%, which may be attributed to unknown systematics in Gaia's data taken at different epochs or albedo variegations on Agamemnon's surface.

As mentioned in Section 1, Agamemnon is considered the third-largest known Trojan, being behind (624) Hektor and (617) Patroclus. Our nonconvex model for Agamemnon yields a surface-equivalent diameter of 156.0 ± 7.8 km. These values suggest that Agamemnon may be larger than the Patroclus–Menoetius binary system, which has an estimated combined equivalent diameter of 140.36 ± 0.87 km by T. Grav et al. (2012), 140.85 ± 3.37 km by F. Usui et al. (2011), and 143.14 ± 8.37 km by B. Carry (2012). A stellar occultation by Patroclus–Menoetius has also been observed, yielding volume-equivalent diameters of 113 km for Patroclus and 104 km for Menoetius, which combine into an area-equivalent diameter of 154 km (M. W. Buie et al. 2015).

Table 6
New Astrometric Positions for Agamemnon Considering the Reference at the Geocenter (ICRS)

Date/Time	R.A. (mas) decl. (mas)	Center X (km) Center Y (km)
2020-10-02	23 43 47.6818992 ± 2.482	6.0 ± 7.4
23:42:44.300	11 00 06.539031 ± 3.048	−10.4 ± 9.0
2022-10-26	5 23 58.0469209 ± 0.438	21.4 ± 1.3
17:53:51.800	48 20 06.515166 ± 0.443	−1.0 ± 1.3
2022-11-02	5 21 17.1054546 ± 1.367	25.4 ± 4.1
23:53:40.960	48 44 14.854499 ± 2.425	−6.6 ± 7.4
2022-11-06	5 19 39.7878133 ± 2.752	18.8 ± 8.4
10:27:27.860	48 54 15.605095 ± 11.802	−18.7 ± 35.9
2022-11-20	5 11 13.9533853 ± 0.371	13.8 ± 1.1
04:03:48.000	49 22 27.678091 ± 6.570	24.6 ± 19.5
2023-02-12	4 30 20.3495166 ± 0.824	29.1 ± 2.7
18:26:29.240	44 58 06.541104 ± 0.660	1.3 ± 2.1
2023-12-16	8 29 48.2980230 ± 0.132	20.3 ± 0.3
11:28:21.000	38 16 06.195517 ± 0.205	−14.3 ± 0.5
2024-03-05	7 42 42.0497859 ± 0.619	25.1 ± 1.9
21:09:51.680	37 14 03.936663 ± 1.120	−23.2 ± 3.5
2024-03-26	7 41 09.9566579 ± 9.261	35.3 ± 30.5
01:00:13.500	35 46 29.887879 ± 5.092	−112.4 ± 5.9
2024-03-27	7 41 20.6820807 ± 9.396	−0.5 ± 32.5
18:57:09.060	35 38 22.298222 ± 3.682	−10.6 ± 12.7
2024-11-29	10 30 41.8832228 ± 0.149	14.4 ± 0.1
03:45:06.760	16 09 04.079141 ± 0.172	−10.6 ± 0.3
2025-03-02	10 02 00.7849697 ± 8.045	17.3 ± 25.0
11:31:09.560	16 24 02.805726 ± 17.158	−25.3 ± 53.4

Note. Uncertainties given in milliarcseconds, in δ(R.A.). cos(Decl.) for the R.A. and δ(Decl.) for the decl. The "Center X" and "Center Y" represent the difference between the predicted (using JPL#132 ephemeris) and obtained centers in kilometers for the stellar occultation events projected on the sky plane.

By considering stellar occultation events and 3D models, we can also derive the body's astrometric positions at each event epoch. Table 6 shows the new geocentric astrometric (ICRS) positions considering the center obtained with the nonconvex model at the occultation times.

7. Conclusions

We obtained 22 new stellar occultation chords on (911) Agamemnon from 12 different events, 1 new rotational light curve obtained at Pico dos Dias Observatory, which, combined with the other 4 curves provided by ALCDEF and 2 solar phase angle curves, allowed us to evaluate the quality of Agamemnon's 3D model provided by DAMIT. It showed that the overall quality of the model is reasonable, but it could be improved to better reproduce the new data. The application of the χ^2 test to compare the observed and synthetic light curves, along with the χ^2_{occ} test, provided new constraints for Agamemnon's model proposed by DAMIT (Tables 2 and 3).

Using ADAM software, we created a new nonconvex 3D model of Agamemnon, which enhanced our understanding of its physical structure, rotational properties, and reflective characteristics. By comparing the obtained model with the rotational light

curves and solar phase angle curves using a χ^2 test, we were able to rigorously assess their uncertainties, resulting in pole orientations of $\lambda = 128.^{\circ}1 \pm 0.^{\circ}8$ and $\beta = 2.^{\circ}3 \pm 2.^{\circ}1$, as well as a rotation period of 6.581797 ± 0.000003 hr. By comparing the model with the occultation chords, using the $\chi^2_{\rm occ}$ test, we could determine the model's scale uncertainty with a $\sigma_{\rm model}$ of 3 km, resulting in a volumetric-equivalent diameter of 151.3 ± 7.6 km and a surface-equivalent diameter of 156.0 ± 7.8 km, providing a geometric albedo of $p_{\rm G} = 0.051 \pm 0.005$. These results also indicate that (911) Agamemnon may be the second largest Jupiter Trojan, being smaller than (624) Hektor and larger than (617) Patroclus.

8. Software and Third Party Data Repository Citations

This work uses data obtained from the Asteroid light curve Data Exchange Format (ALCDEF) database, which is supported by funding from NASA grant 80NSSC18K0851.

This work has made use of data from the European Space Agency (ESA) mission Gaia (https://www.cosmos.esa.int/gaia), processed by the Gaia Data Processing and Analysis Consortium (DPAC; https://www.cosmos.esa.int/web/gaia/dpac/consortium). Funding for the DPAC has been provided by national institutions, in particular the institutions participating in the Gaia Multilateral Agreement.

This work made use of the Database of Asteroid Models from Inversion Techniques (DAMIT; J. Durech et al. 2010), which provides shape models and spin-state solutions for solar system small bodies.

This work also used the All-Data Asteroid Modeling software developed by M. Viikinkoski et al. (2015) to derive three-dimensional models from multiple observation techniques.

Acknowledgments

This study was financed in part by the Coordenação de Aperfeiçoamento de Pessoal de Nível Superior—Brasil (CAPES)—Finance Code 001 and National Institute of Science and Technology of the e-Universe project (INCT do e-Universo, CNPq grant 465376/2014-2). E.O.G. acknowledges the CAPES-DS scholarship. F.B.R. acknowledges CNPq grant 316604/2023-2 and the financial support of the NAPI "Fenômenos Extremos do Universo" of Fundação de Apoio à Ciência, Tecnologia e Inovação do Paraná (Fundação Araucária). A.R.G.J. is thankful for the financial support of FAPEMIG APQ-02987-24 and CNPQ 408543/2025-6. B.S. acknowledges support by the French ANR project Roche, number ANR-23-CE49-0012. C.L.P. thanks the FAPERJ/DSC-10 E-26/204.141/2022, FAPERJ/PDR-10 E-26/200.107/2025, and FAPERJ 200.108/2025. This work was partly funded by the Spanish projects PID2020-112789GBI00 (AEI) and Proyecto de Excelencia de la Junta de Andalucía PY20-01309. J.L.O., P.S.-S., Y.K., and N.M. acknowledge financial support from the Severo Ochoa grant CEX2021-001131-S (MCIN/AEI/10.13039/501100011033). P.S.-S. and Y.K. also acknowledge support from the Spanish I+D+i project PID2022-139555NB-I00 funded by MCIN/AEI/10.13039/501100011033. B.E.M. is thankful for CNPq grant 408543/2025-6 and CAPES grant 23079.212658/2024-30. L.M.C. is thankful to CAPES for the financial support, Finance Code 001, and CAPES/PDSE grant 88881.981125/2024-01. L.L. acknowledges the project Gaia Moons of the Agence Nationale de Recherche (France), grant ANR-22-CE49-0002. A.J.C.T. acknowledges support from the Spanish Ministry project PID2023-151905OB-I00 and Junta de Andalucía grant P20_010168. M.G. acknowledges the Academy of Finland project no. 325806 (PlanetS). The program of development within Priority-2030 is acknowledged for supporting the research at UrFU. E.S. thanks the Adiyaman University Astrophysics Application and Research Center for their support in the acquisition of data with the ADYU60 telescope. A.M. acknowledges the National Science Centre, Poland, through grant No. 2020/39/O/ST9/00713. The authors acknowledge the use of the Occultation Portal, whose hosting, maintenance, and infrastructure are supported by the Paris Astronomical Data Centre (PADC), the Direction Informatique de l'Observatoire de Paris (DIO), the Instituto de Astrofísica de Andalucía (IAA-CSIC), and the Federal University of Technology - Paraná (UTFPR-Curitiba). Some results presented in this work were obtained at the Pico dos Dias Observatory using the 0.6 m telescope (IAG), operated by the National Laboratory of Astrophysics (LNA/Brazil). Part of the data processing was carried out using computers provided by the Interinstitutional Laboratory of e-Astronomy (LIneA/Brazil). IST60 and IST40 are the observational facilities of the Istanbul University Observatory that were funded by the Scientific Research Projects Coordination Unit of Istanbul University with project numbers BAP-3685 and FBG-2017-23943 and the Presidency of Strategy and Budget of Republic of Turkey with the project 2016K12137.

Appendix
Stellar Occultation Information

For each stellar occultation event, the star position, G magnitude, and apparent diameter in the *V* band are presented in Table 7. The observers' information for each campaign is displayed in Table 8, along with the immersion and emersion times obtained for the occultations. As explained in Section 2.2, these times are obtained by modeling the obtained occultation light curve. The resulting light curves and the model are shown in Figures 9 and 10.

Table 7
Star Information for Each Event

Event date	Gaia Source ID	R.A. (mas) Decl. (mas)	Magnitude (G)	Apparent Diameter V (mas)
2020 Oct 2	2763530430972916736	234347.69716 ± 0.0118 110005.6765 ± 0.0103	13.293	0.0292
2022 Oct 26	212613873431311360	52358.02984 ± 0.0143 482006.4959 ± 0.0124	13.834	0.0166
2022 Nov 2	213434074746535552	52117.08575 ± 0.0217 484414.7539 ± 0.0174	14.875	0.0135
2022 Nov 6	213266330503331328	51939.78288 ± 0.0169 485415.5353 ± 0.0148	14.289	0.0116
2022 Nov 20	261339620274262400	51113.95239 ± 0.0137 492227.6538 ± 0.0091	13.388	0.0180
2023 Feb 12	253561026483846400	43020.33956 ± 0.0196 445806.5428 ± 0.0097	14.686	0.0125
2023 Mar 20	203729265426450688	44826.92122 ± 0.0428 423628.9736 ± 0.0281	16.095	0.0069
2023 Dec 16	911145395945237760	82948.30374 ± 0.0116 381606.2479 ± 0.0094	13.177	0.0202
2024 Mar 5	895891321378187264	74242.07177 ± 0.0326 371403.8374 ± 0.0234	15.757	0.0075
2024 Mar 26	895654617139555584	74109.84468 ± 0.4354 354629.6143 ± 0.3079	14.363	0.0122
2024 Mar 27	894527102326136320	74120.66118 ± 0.0164 353822.3293 ± 0.0123	14.205	0.0146
2024 Nov 29	3889297949742037248	103041.86980 ± 0.0176 160903.5946 ± 0.0141	13.836	0.0128
2025 Mar 2	622728824371056384	100200.78101 ± 0.0449 162401.5439 ± 0.0484	16.069	0.0065

Note. The prediction map and details of each event can be accessed by clicking on the event date.

Table 8
Observer Information

Site Name Country Principal Observer Name	Latitude Longitude Altitude (m)	Camera Exposure Time (s)	Status Immersion Time (s) Emersion Time (s)
2020 Oct 2			
İST40 Türkiye Süleyman Fişek	41° 0′ 42.2964″ N 28° 57′ 56.5848″ E 60.00	Moravian G2 8300 0.500	Positive 2020-10-02 23:39:03.77 ± 1.29 2020-10-02 23:39:10.74 ± 1.27
INTA Spain Alberto Javier Castro-Tirado	37° 6′ 14.7492″ N 6° 44′ 2.8032″ W 53.00	Andor iXon-897 2.000	Positive 2020-10-02 23:41:45.71 ± 0.17 2020-10-02 23:41:49.60 ± 0.71
Albox Spain Jose Luis Maestre Garcia	37° 24′ 20.0016″ N 2° 9′ 6.0012″ W 486.00	Camera: Atik 314L+ (Sony ICX-285AL) 2.500	Negative … …
Turksat Türkiye Mehmed Naim Bağıran	39° 38′ 11.8752″ N 32° 48′ 14.9652″ E 950.00	FLI 0.300	Negative … …
Selami Kalkan Türkiye Ondokuz Mayis	41° 22′ 3.8172″ N 36° 12′ 5.6736″ E 150.00	SBIG STL-4020M CCD …	Overcast … …
İST60 Türkiye Oğuzhan Çakir	40° 5′ 56.364″ N 26° 28′ 28.164″ E 410.00	Andor iXon Ultra 888 …	Technical failure … …
Ibiza (TCH) Spain Ignacio de la Cueva Torregrosa	38° 53′ 27.9996″ N 1° 14′ 26.9988″ E 793.00	SBIG STL-11000 2.0	Technical failure … …
2022 Oct 26			
Chalin Poland Anna Marciniak	52° 36′ 14.027″ N 16° 2′ 33.4403″ E 65.00	Andor Zyla 5.5 sCMOS 0.600	Positive 2022-10-26 18:03:26.98 ± 0.16 2022-10-26 18:03:38.52 ± 0.14
Roof Observatory Kaufering Germany Gregor Krannich	48° 5′ 22.7793″ N 10° 50′ 57.9958″ E 596.00	QHY174M-GPS 0.400	Positive 2022-10-26 18:03:48.83 ± 0.22 2022-10-26 18:03:59.37 ± 0.25
2022 Nov 2			
Westport Astronomical Society United States Kevin Green	41° 10′ 15.8999″ N 73° 19′ 39.2999″ W 88.00	QHY174M-GPS 0.750	Positive 2022-11-03 00:02:26.93 ± 0.26 2022-11-03 00:02:40.98 ± 0.28
2022 Nov 6			
Eisenhower State Park United States Steve Messner	38° 31′ 2.496″ N 95° 44′ 58.344″ W 327.00	WAT-910 HX-RC 0.264	Positive 2022-11-06 10:24:14.55 ± 0.55 2022-11-06 10:24:26.07 ± 0.38
2022 Nov 20			
Nikitin Home United States Vadim Nikitin	40° 4′ 8.60999″ N 105° 11′ 0.96″ W 1594.00	QHY174 GPS 0.250	Positive 2022-11-20 04:08:46.77 ± 0.06 2022-11-20 04:08:56.80 ± 0.04
John Beckman Obsevatory Spain Antonio Santiago Amado	36° 50′ 59.5536″ 2° 17′ 21.5808″ 60.00	ST8XME 4.000	Positive 2022-11-20 04:00:04.68 ± 3.56 2022-11-20 04:00:13.22 ± 3.39
La Hita Observatory Spain Nicolás Morales	39° 34′ 7.014″ N 3° 11′ 9.816″ W 675.00	SBIG STX11000 4.000	Negative … …
2023 Feb 12			
Sternwarte Eberfing	47° 47′ 43.8″ N	IMX174 DVTI	Positive

Table 8
(Continued)

Site Name Country Principal Observer Name	Latitude Longitude Altitude (m)	Camera Exposure Time (s)	Status Immersion Time (s) Emersion Time (s)
Germany Martin Gutekunst	11° 12′ 15.3″ E 618.00	0.500	2023-02-12 18:26:05.72 ± 0.17 2023-02-12 18:26:20.57 ± 0.12
2023 Mar 20			
Sant Esteve Sesrovires Spain Carles Schnabel	41° 29′ 36.996″ N 1° 52′ 21″ E 180.00	Watec 910 HX/RC 2.560	Negative … …
2023 Dec 16			
Nikitin Mobile United States Vadim Nikitin	36° 39′ 45.7679″ N 104° 29′ 46.2937″ W 1849.40	QHY174 GPS 0.125	Positive 2023-12-16 11:25:38.77 ± 0.04 2023-12-16 11:25:47.70 ± 0.05
Barton Observatory United States Johnny Barton	31° 24′ 47.952″ N 97° 5′ 4.62001″ W 141.00	RunCam Night Eagle 2 Astro 0.033	Positive 2023-12-16 11:24:28.39 ± 0.06 2023-12-16 11:24:40.25 ± 0.03
Eisfeldt Observatory United States James Eisfeldt	31° 37′ 44.6196″ N 97° 14′ 59.7912″ W 161.00	RunCam Night Eagle Astro 0.132	Positive 2023-12-16 11:24:30.73 ± 0.09 2023-12-16 11:24:42.20 ± 0.10
2024 Mar 5			
Southside Observatory United Kingdom Tim Haymes	51° 55′ 40.296″ N 1° 18′ 47.16″ W 122.00	QHY174M GPS 0.600	Positive 2024-03-05 21:07:36.86 ± 0.31 2024-03-05 21:07:45.40 ± 0.18
2024 Mar 26			
Sternwarte Comthurey Germany Konrad Guhl	53° 15′ 57.888″ N 13° 11′ 24.576″ E 74.00	QHY174M GPS 0.500	Positive 2024-03-26 00:54:59.97 ± 0.25 2024-03-26 00:55:13.76 ± 0.20
2024 Mar 27			
Sternwarte Comthurey Germany Konrad Guhl	53° 15′ 57.888″ N 13° 11′ 24.576″ E 74.00	QHY174M GPS 0.400	Positive 2024-03-27 18:54:33.41 ± 0.16 2024-03-27 18:54:48.34 ± 0.11
Elianto II Italy Alfonso Noschese	40° 38′ 40.56″ N 14° 52′ 43.32″ E 40.00	DVTI+CAM 430 0.200	Negative … …
Ondrejov Cosmic Lab roof Czech Republic Jan Mánek	49° 54′ 36.2016″ N 14° 46′ 47.7012″ E 524.00	DVTI+CAM 430 …	Overcast … …
2024 Nov 29			
ADYU60 Türkiye Eda Sonbas	37° 45′ 6.0012″ N 38° 13′ 31.0008″ E 675.00	Andor Tech ikon-M 934 1.000	Positive 2024-11-29 03:43:28.59 ± 1.62 2024-11-29 03:43:34.18 ± 1.79
İST40 Türkiye Süleyman Fişek	41° 0′ 42.2964″ N 28° 57′ 56.5848″ E 60.00	Moravian G2 8300 1.000	Positive 2024-11-29 03:41:59.56 ± 1.56 2024-11-29 03:42:08.53 ± 1.58
Hamsey Green United Kingdom Malcolm Jennings	51° 19′ 9.516″ N 0° 4′ 1.524″ W 170.00	Watec 910 HX 0.320	Positive 2024-11-29 03:38:06.81 ± 0.17 2024-11-29 03:38:20.41 ± 0.45
Cottered Observatory United Kingdom Simon Kidd	51° 57′ 4.3992″ N 0° 3′ 51.6996″ W 120.00	ZWO ASI432 MM 0.104	Positive 2024-11-29 03:38:04.90 ± 0.01 2024-11-29 03:38:19.62 ± 0.11
Ruvonia Belgium	50° 5′ 40.056″ N 5° 2″ 42.144′ E	DVTI-CAM 430 1.000	Positive 2024-11-29 03:38:37.91 ± 0.36

Table 8
(Continued)

Site Name Country Principal Observer Name	Latitude Longitude Altitude (m)	Camera Exposure Time (s)	Status Immersion Time (s) Emersion Time (s)
Jean Bourgeois	213.00		2024-11-29 03:38:52.07 ± 0.30
Peter Tickner Home United Kingdom Peter Tickner	51° 25′ 33.4092″ N 0° 55′ 14.7648″ W 44.00	ZWO ASI432 MM 0.250	Positive 2024-11-29 03:38:02.02 ± 0.02 2024-11-29 03:38:15.70 ± 0.02
Emmendingen Germany Germany Karl–Ludwig Bath	48° 6′ 14.2057″ N 7° 51′ 28.4179″ E 210.54	ZWO ASI174MM 0.750	Negative … …
Cugnasco-Gerra Switzerland Andrea Manna	46° 10′ 35.544″ N 8° 55′ 13.8″ E 240.00	Watec 910 HX/RC 1.280	Negative … …
Gnosca Switzerland Stefano Sposetti	46° 13′ 53.1084″ N 9° 1′ 26.616″ E 258.88	QHY174M-GPS 0.300	Negative … …
Southside Observatory United Kingdom Tim Haymes	51° 55′ 40.296″ N 1° 18′ 47.16″ W 122.00	QHY174M-GPS …	Overcast … …
TURKSAT Türkiye Mehmed Naim Bağıran	39° 38′ 11.8752″ N 32° 48′ 14.9652″ E 950.00	QHY174M-GPS …	Overcast … …
Ondrejov Cosmic Lab roof Czech Republic Jan Mánek	49° 54′ 36.2016″ N 14° 46′ 47.7012″ E 524.00	DVTI+CAM 430 …	Overcast … …
Tübingen University Germany Christoph Schäfer	48° 32′ 3.0156″ N 9° 4′ 12.0036″ E 400.00	ZWO ASI294MC Pro …	Overcast … …
ISTEK Belde Observatory Türkiye Mert Acar	41° 1′ 49.0476″ N 29° 2′ 33.3996″ E 110.00	QHY 5 III 178 M …	Overcast … …
Schreurs O. Home Belgium Olivier Schreurs	50° 38′ 35.0919″ N 5° 33′ 27.4386″ E 107.00	Watec 910 HX/RC …	Overcast … …
Dourbes Belgium Roland Boninsegna	50° 5′ 25.872″ N 4° 34′ 55.992″ E 192.00	Watec 910 HX …	Overcast … …
2025 Mar 2			
Vadim Nikitin Mobile United States Vadim Nikitin	41° 24′ 28.0062″ N 104° 52′ 38.204″ W 1944.10	QHY174 GPS 1.500	Positive 2025-03-02 11:26:54.72 ± 1.92 2025-03-02 11:27:06.37 ± 1.86

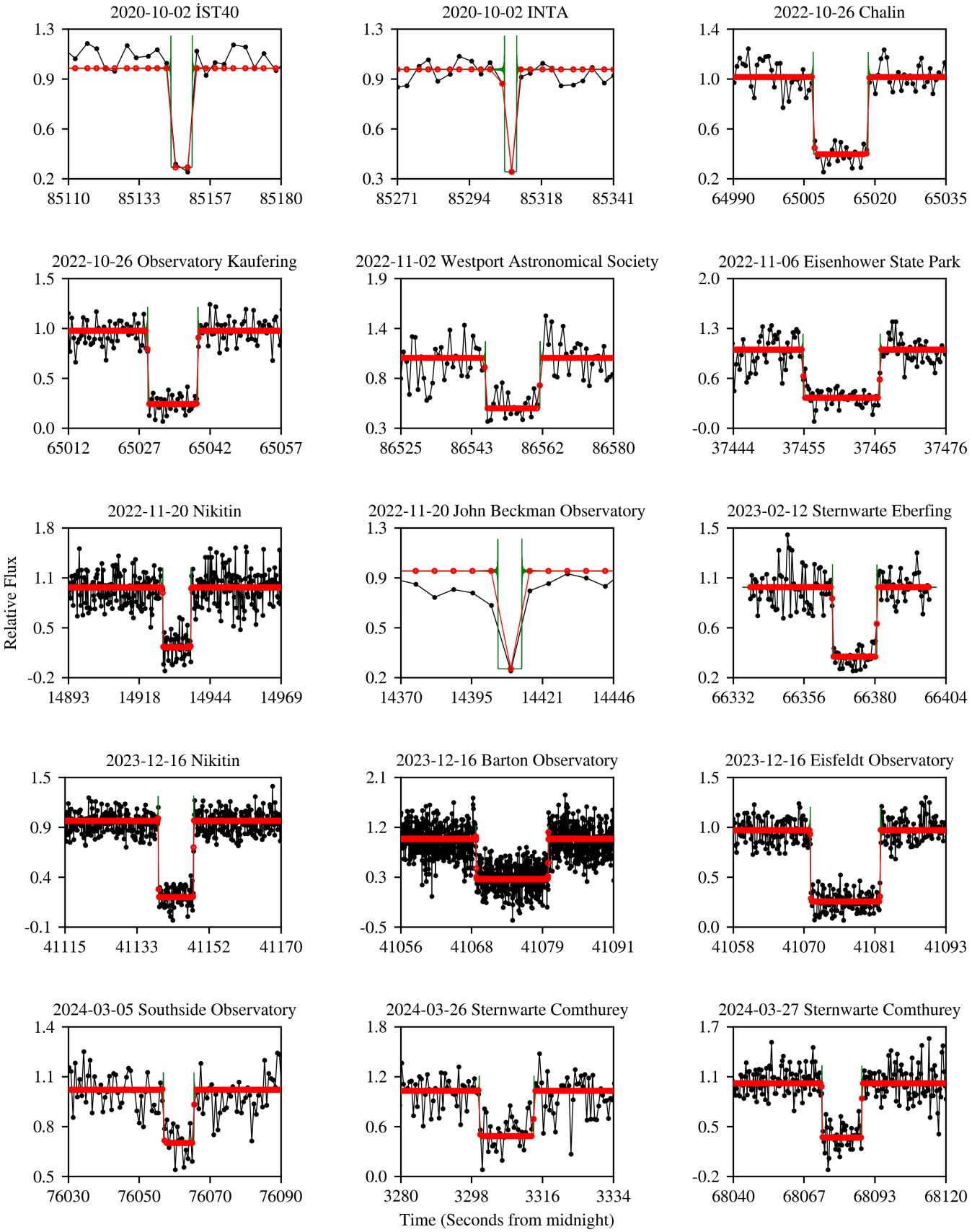


Figure 9. Light curves obtained for the occultation events. Each black dot represents the photometric flux extracted from each image obtained. The green thin line represents the Fresnel diffraction pattern. The red line represents the light-curve model used to determine the event's immersion and emersion times, taking into account the stellar diameter, light diffraction, and the applied exposure time.

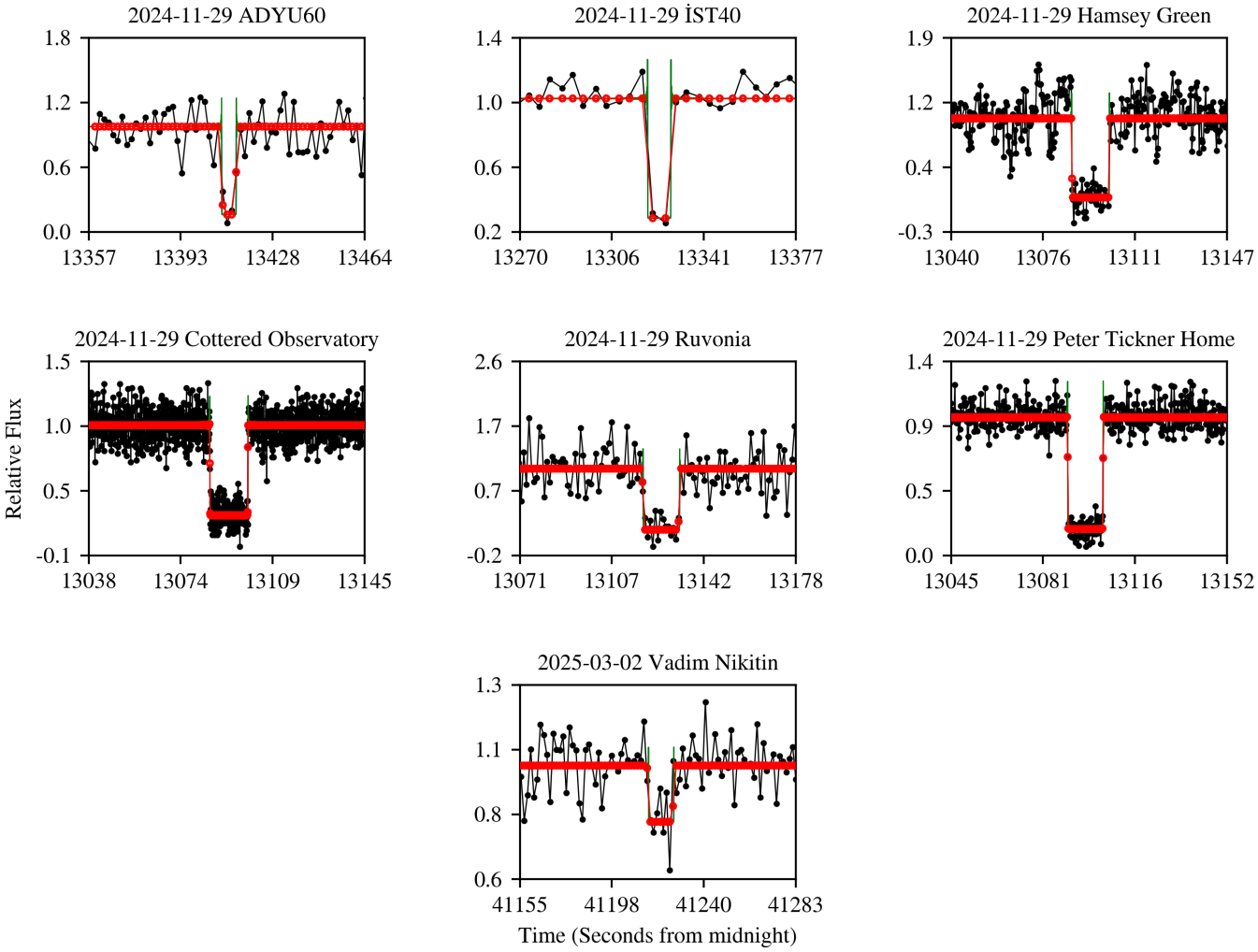


Figure 10. Light curves obtained from the occultation events (see caption of Figure 9).

ORCID iDs

Eros de O. Gradovski https://orcid.org/0009-0001-5754-4688
Felipe Braga-Ribas https://orcid.org/0000-0003-2311-2438
Altair R. Gomes-Junior https://orcid.org/0000-0002-3362-2127
Bruno Sicardy https://orcid.org/0000-0003-1995-0842
Jose Luis Ortiz https://orcid.org/0000-0002-8690-2413
Giuliano Margoti https://orcid.org/0000-0002-2103-4408
Chrystian L. Pereira https://orcid.org/0000-0003-1000-8113
Pablo Santos-Sanz https://orcid.org/0000-0002-1123-983X
Josselin Desmars https://orcid.org/0000-0002-2193-8204
Yucel Kilic https://orcid.org/0000-0001-8641-0796
Nicolás Morales https://orcid.org/0000-0003-0419-1599
Roberto Vieira-Martins https://orcid.org/0000-0003-1690-5704
Rafael Sfair https://orcid.org/0000-0002-4939-013X
Bruno Morgado https://orcid.org/0000-0003-0088-1808
Julio I. B. de Camargo https://orcid.org/0000-0002-1642-4065
Marcelo Assafin https://orcid.org/0000-0002-8211-0777
Fabio A. Spina https://orcid.org/0000-0002-5437-8928
Flavia Rommel https://orcid.org/0000-0002-6085-3182
Gustavo Benedetti-Rossi https://orcid.org/0000-0002-4106-476X
Jonatã Arcas-Silva https://orcid.org/0009-0007-1444-9502
Luan M. Catani https://orcid.org/0000-0002-1960-888X
Luana Liberato https://orcid.org/0000-0003-3433-6269
Patricia Buzzatto https://orcid.org/0000-0001-7361-6445
Thamiris de Santana https://orcid.org/0000-0003-3194-5237
Vadim Nikitin https://orcid.org/0009-0007-7900-4811
Mehmed N. Bağiran https://orcid.org/0000-0002-3220-4871
Suleyman Fisek https://orcid.org/0000-0002-3187-5286
Alberto J. Castro-Tirado https://orcid.org/0000-0003-2999-3563
Alper K. Ates https://orcid.org/0000-0002-8254-6861
Anna Marciniak https://orcid.org/0000-0002-1627-9611
Carles Schnabel https://orcid.org/0009-0000-2929-3909
Christoph M. Schafer https://orcid.org/0000-0002-0341-3738

Eda Sonbas https://orcid.org/0000-0002-6909-192X
Fuat K. Yelkenci https://orcid.org/0000-0003-2675-3564
Jose L. Maestre https://orcid.org/0000-0003-3995-9633
Kevin Green https://orcid.org/0009-0009-8680-5742
Maria Gritsevich https://orcid.org/0000-0003-4268-6277
Mert Acar https://orcid.org/0000-0001-8898-2587
Oguzhan Cakir https://orcid.org/0000-0002-1045-2559
Peter Tickner https://orcid.org/0000-0001-8130-8469
Selami Kalkan https://orcid.org/0000-0002-0854-7858
Sinan Alis https://orcid.org/0000-0002-6990-8899
Waldemar Ogloza https://orcid.org/0000-0002-6293-9940

References

Assafin, M. 2023, P&SS, 239, 105816
Bartczak, P., & Dudziński, G. 2018, MNRAS, 473, 5050
Bowell, E., Oszkiewicz, D. A., Wasserman, L. H., et al. 2014, M&PS, 49, 95
Braga-Ribas, F., Sicardy, B., Ortiz, J. L., et al. 2014, Natur, 508, 72
Buie, M. W., Olkin, C. B., Merline, W. J., et al. 2015, AJ, 149, 113
Carry, B. 2012, P&SS, 73, 98
Carry, B., Dumas, C., Kaasalainen, M., et al. 2010, Icar, 205, 460
Casagrande, L., & VandenBerg, D. A. 2018, MNRAS: Letters, 479, L102
Desmars, J., Camargo, J. I. B., Braga-Ribas, F., et al. 2015, A&A, 584, A96
Ďurech, J., Hanuš, J., & Vančo, R. 2019, A&A, 631, A2
Durech, J., Sidorin, V., & Kaasalainen, M. 2010, A&A, 513, A46
Fortin, F.-A., De Rainville, F.-M., Gardner, M.-A., Parizeau, M., & Gagné, C. 2012, JMLR, 13, 2171
Gaia Collaboration, Spoto, F., Tanga, P., et al. 2018, A&A, 616, A13
Gomes, R., Levison, H. F., Tsiganis, K., & Morbidelli, A. 2005, Natur, 435, 466
Gomes-Júnior, A. R., Assafin, M., Braga-Ribas, F., et al. 2019, MNRAS, 492, 770
Gomes-Júnior, A. R., Morgado, B. E., Benedetti-Rossi, G., et al. 2022, MNRAS, 511, 1167
Grav, T., Mainzer, A. K., Bauer, J. M., Masiero, J. R., & Nugent, C. R. 2012, ApJ, 759, 49
Kaasalainen, M., & Lamberg, L. 2006, InvPr, 22, 749
Kaasalainen, M., & Torppa, J. 2001, Icar, 153, 24
Kaasalainen, M., Torppa, J., & Muinonen, K. 2001, Icar, 153, 37
Kilic, Y., Braga-Ribas, F., Kaplan, M., et al. 2022, MNRAS, 515, 1346
Levison, H. F., Olkin, C. B., Noll, K. S., et al. 2021, PSJ, 2, 171
Levison, H. F., Shoemaker, E. M., & Shoemaker, C. S. 1997, Natur, 385, 42
Li, J., Xia, Z. J., Yoshida, F., Georgakarakos, N., & Li, X. 2023, A&A, 669, A68
Marchis, F., Durech, J., Castillo-Rogez, J., et al. 2014, ApJ, 783, L37
Marzari, F., & Scholl, H. 1998, Icar, 131, 41
Morbidelli, A., Levison, H. F., Tsiganis, K., & Gomes, R. 2005, Natur, 435, 462
Morgado, B. E., Sicardy, B., Braga-Ribas, F., et al. 2023, Natur, 614, 239
Nesvorný, D., Vokrouhlický, D., & Morbidelli, A. 2013, ApJ, 768, 45
Noll, K. S., Brown, M. E., Weaver, H. A., et al. 2020, PSJ, 1, 44
Olkin, C. B., Levison, H. F., Vincent, M., et al. 2021, PSJ, 2, 172
Ortiz, J. L., Santos-Sanz, P., Sicardy, B., et al. 2017, Natur, 550, 219
Oszkiewicz, D., Muinonen, K., Bowell, E., et al. 2011, JQSRT, 112, 1919
Pereira, C. L., Braga-Ribas, F., Sicardy, B., et al. 2025, ApJL, 992, L19
Pereira, C. L., Sicardy, B., Morgado, B. E., et al. 2023, A&A, 673, L4
Polakis, T. 2021, MPBu, 48, 144
Rommel, F. L., Braga-Ribas, F., Ortiz, J. L., et al. 2023, A&A, 678, A167
Sicardy, B., Braga-Ribas, F., Buie, M. W., Ortiz, J. L., & Roques, F. 2024, A&ARv, 32, 6
Sicardy, B., Ortiz, J. L., Assafin, M., et al. 2011, Natur, 478, 493
Stephens, R. D. 2009, MPBu, 36, 59
Stephens, R. D., & Warner, B. D. 2021, MPBu, 48, 13
Timerson, B., Brooks, J., Conard, S., et al. 2013, P&SS, 87, 78
Tsiganis, K., Gomes, R., Morbidelli, A., & Levison, H. F. 2005, Natur, 435, 459
Usui, F., Kuroda, D., MÜLler, T. G., et al. 2011, PASJ, 63, 1117
Viikinkoski, M., Kaasalainen, M., & Durech, J. 2015, A&A, 576, A8
Willmer, C. N. A. 2018, ApJS, 236, 47